Available online at www.sciencedirect.com
ScienceDirect
Trans. Nonferrous Met. Soc. China 27(2017) 1677−1688
Transactions of Nonferrous Metals Society of China
www.tnmsc.cn

Characterization of hot deformation behavior of AA2014 forging aluminum alloy using processing map

Peng-wei LI[1], Hui-zhong LI[1,2,3], Lan HUANG[3], Xiao-peng LIANG[1,2], Ze-xiao ZHU[1]

1. School of Materials Science and Engineering, Central South University, Changsha 410083, China;
2. Key Laboratory of Nonferrous Metal Materials Science and Engineering, Ministry of Education, Central South University, Changsha 410083, China;
3. State Key Laboratory of Powder Metallurgy, Central South University, Changsha 410083, China

Received 11 July 2016; accepted 4 January 2017

Abstract: The hot deformation behavior of AA2014 forging aluminum alloy was investigated by isothermal compression tests at temperatures of 350−480 °C and strain rates of 0.001−1 s^{-1} on a Gleeble−3180 simulator. The corresponding microstructures of the alloys under different deformation conditions were studied using optical microscopy (OM), electron back scattered diffraction (EBSD) and transmission electron microscopy (TEM). The processing maps were constructed with strains of 0.1, 0.3, 0.5 and 0.7. The results showed that the instability domain was more inclined to occur at strain rates higher than 0.1 s^{-1} and manifested in the form of local non-uniform deformation. At the strain of 0.7, the processing map showed two stability domains: domain I (350−430 °C, 0.005−0.1 s^{-1}) and domain II (450−480 °C, 0.001−0.05 s^{-1}). The predominant softening mechanisms in both of the two domains were dynamic recovery. Uniform microstructures were obtained in domain I, and an extended recovery occurred in domain II, which would lead to the potential sub-grain boundaries progressively transforming into new high-angle grain boundaries. The optimum hot working parameters for the AA2014 forging aluminum alloy were determined to be 370−420 °C and 0.008−0.08 s^{-1}.
Key words: AA2014 aluminum alloy; hot deformation behavior; constitutive model; processing map; softening mechanism

1 Introduction

AA2014 aluminum alloy, as a kind of forging alloy, is one of the most important aeronautical materials owing to the excellent combination properties of high strength, high toughness and good corrosion resistance [1,2]. The aeronautical forgings such as aircraft landing gear hub and engine components have been extensively applied. The production of such forgings undergoes complex processing steps like cogging and die forging. However, the flaws may be generated during deformation owing to narrow forging temperature range and unstable forged microstructure. Controlling the forging processes to attain a uniform microstructure seems to be very important. Thus, it needs a comprehensive understanding of the hot deformation behavior of the alloy to develop a reasonable forging process.

In recent years, the Arrhenius equation has been adopted extensively to research the effect of deformation conditions on the flow behavior and microstructure evolution and to reveal the relationship between Zener−Hollomon parameters and dynamic softening mechanism of aluminum alloys. Those studies generally suggested that the flow stresses diminish with rising the deformation temperature and decreasing strain rates [3−5]. Moreover, considerable researches have shown that dynamic recrystallization (DRX) occurs in aluminum alloy during hot deformation, and the occurrence of DRX must be below or equal to a critical Z value [6−8].

It is worth emphasizing that the processing map is also useful for optimizing hot working processes. JIN et al [9] developed the processing maps of a 7050 aluminum alloy and obtained an optimum window (410−460 °C, 10^{-4}−10^{-3} s^{-1}) for the reasonable continuous dynamic recrystallization with the power efficiency of about 50%. LIN et al [10] investigated the hot working of 7075 alloy with the help of processing

Foundation item: Project (51301209) supported by the National Natural Science Foundation of China
Corresponding author: Hui-zhong LI; Tel: +86-731-88830377; Fax: +86-731-88876692; E-mail: lhz606@csu.edu.cn
DOI: 10.1016/S1003-6326(17)60190-0

map and pointed out a domain with coarse precipitates distributed in the grain interior and at boundaries, which may lead to the deep inter-granular corrosion and large areas of denudation layer. LI et al [11] found that the main softening mechanism of an Al−Cu−Li−Sc−Zr alloy was dynamic recovery (DRV) at 440 °C, 0.1 s^{-1} and the DRX could be easily observed at 470 °C and 0.001 s^{-1}.

Up till now, most researchers focus on the research of the flow behavior and the corresponding softening mechanism. While there are only few reports on obtaining a uniform and fine grain size microstructure by utilizing constitutive equation and processing map. Meanwhile, the hot deformation behavior of AA2014 aluminum alloy also needs to be further studied. Thus, in the present study, a strain revised constitutive model was used to investigate the flow behavior of the AA2014 aluminum alloy. And the softening mechanism was studied by microstructure observation. More importantly, an optimum window with single softening mechanism and uniform microstructure was established by the processing map as well as the activation energy.

2 Experimental

The experimental material in the isothermal compression tests was AA2014 aluminum alloy, which was industrially homogenized at 490 °C for 12 h and air cooled. Its chemical composition is listed in Table 1. The original microstructure and the distribution of the second phase particles are shown in Fig. 1. According to the analysis of EDS, particles in bright color with greater percentage are Al_2Cu (θ) phases, and the gray color particles are impurity phase Al−Fe−Mn−Si, while the dark dots on the bright θ phases are Al−Cu−Mg−Si phases. Also, the fine dispersion particles are precipitates during the slow cooling of homogenization.

Table 1 Chemical composition of AA2014 aluminum alloy (mass fraction, %)

Cu	Mg	Si	Mn	Fe	Ga
4.41	0.69	0.64	0.52	0.12	0.028
Zn	Ti	V	P	Al	
0.011	0.014	0.013	0.014	Bal.	

In order to investigate the hot compression behavior of AA2014 aluminum alloy, isothermal compression tests were carried out on a Gleeble−3180 simulator at the deformation temperatures of 350, 400, 450 and 480 °C, the strain rates of 0.001, 0.01, 0.1 and 1 s^{-1}, and the strain up to 0.7. Cylindrical compression specimens were machined with a size of 10 mm in diameter and 15 mm in height. A thermocouple was welded on the specimen to ensure a continuous temperature measurement during the entire heating, deformation and quenching cycle. Cylindrical specimens prior to isothermal compression were heated to deformation temperatures at a heating rate of 5 °C/s and held for 3 min. After compression, the specimens were quenched to room temperature immediately to maintain the deformation microstructures. The deformed specimens were sectioned parallel to the compression axis along the direction of centerline for OM and TEM observation. Metallographic specimens were etched in a Keller's agent. TEM specimens were electro-polished by the twin-jet electro-polishing method using a solution of 70% CH_3OH and 30% HNO_3 at −30 °C. Microstructure observations were performed on a Tecnai $G^2$20 TEM and a Sirion 200 field emission gun SEM, equipped with EBSD detector and Channel 5 software and the parameters used were as follows: accelerating voltage 25 kV, step size 3 μm.

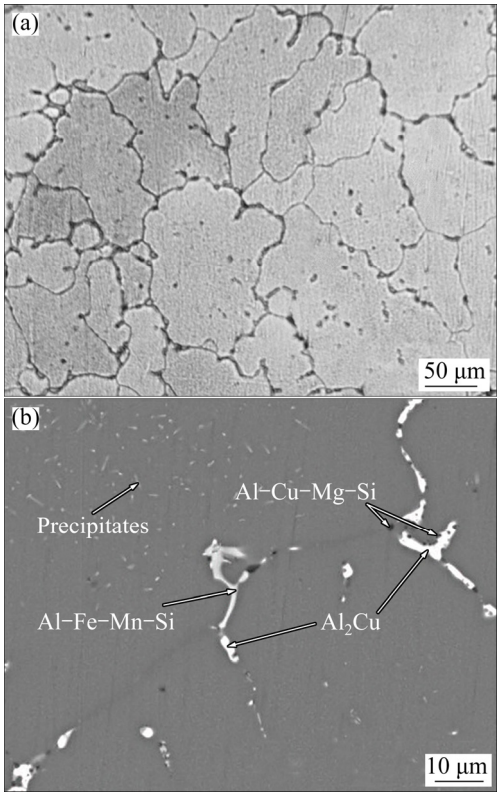

Fig. 1 Initial microstructures of AA2014 aluminum alloy: (a) OM; (b) SEM

3 Results and discussion

3.1 True stress−strain curves

The true stress−strain curves obtained during the isothermal compression tests are shown in Fig. 2. As can be seen from the flow curves, the effects of deformation temperature and strain rate on the flow stress are significant under all the test conditions. The stress level decreases with increasing deformation temperature and decreasing strain rate. The flow stresses rise rapidly and

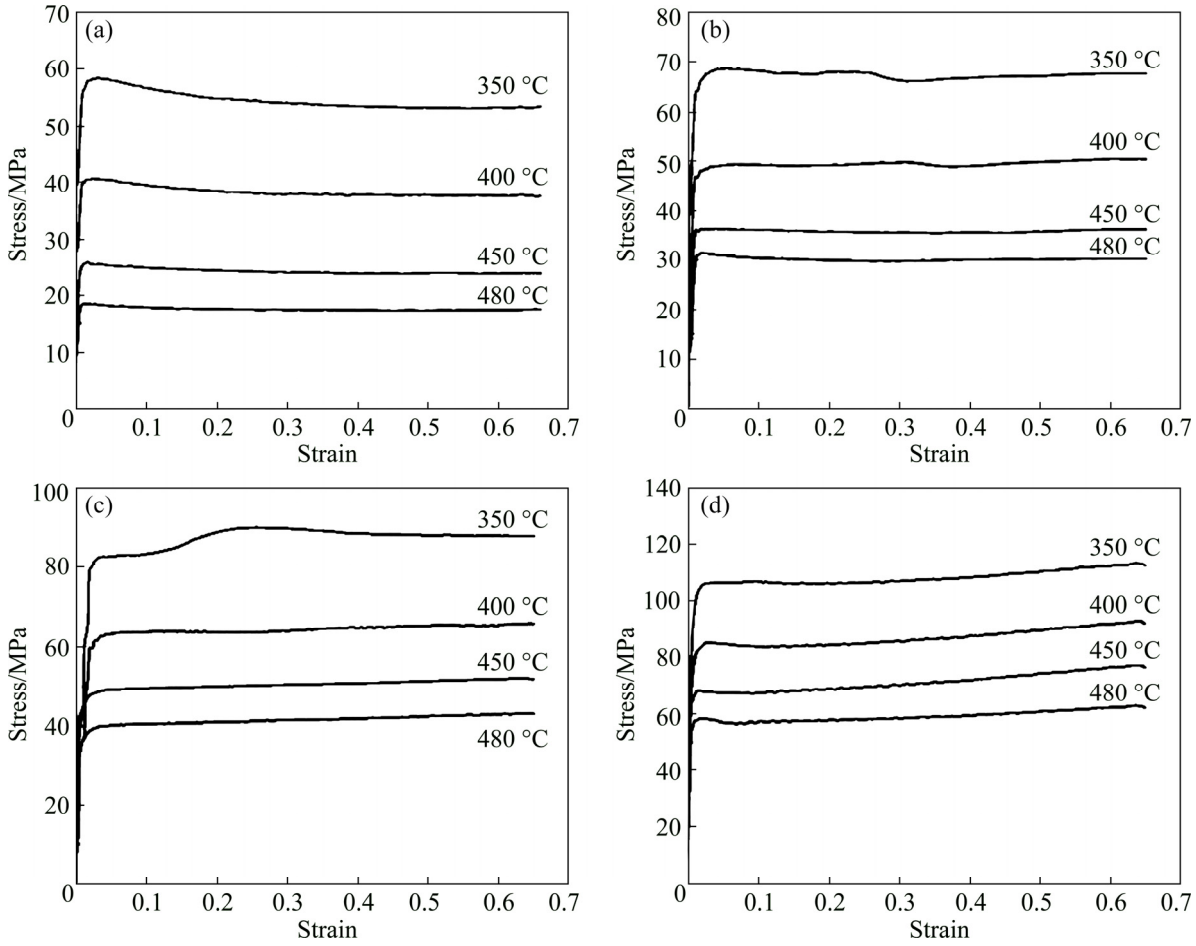

Fig. 2 True stress−true strain curves of AA2014 alloy at different strain rates: (a) 0.001 s^{-1}; (b) 0.01 s^{-1}; (c) 0.1 s^{-1}; (d) 1 s^{-1}

then hold almost constant or decrease slightly after reaching the peak values with increasing strain, suggesting a balance between work hardening and dynamic softening. The deformation at elevated temperature is a competitive process of the dynamic softening and work hardening. At the beginning of the deformation, dislocation density increases dramatically, leading to the rapid increase of stress. As the deformation proceeds, the dynamic softening such as DRV or DRX occurs, which can offset or partially offset the effect of work hardening. Then, the true stress keeps unchanged or declines slightly with the true strain rising.

3.2 Processing maps

Processing map based on the dynamic materials model (DMM) is considered to be an important model for optimizing the hot working parameters and controlling microstructure [12]. According to Prasad's theory, the hot deformation work could be considered as power dissipation. The total power P consists of two complementary parts: G represents the power dissipation through plastic deformation; J represents the power dissipation through microstructure transition, such as DRV, DRX, super-plastic flow, phase transformations as well as damage of the material.

The contents G and J can be related by the strain rate sensitivity parameter m, which is given as follows [13]:

$$m=\left(\frac{\partial J}{\partial G}\right)_{\varepsilon,T}=\frac{\partial J}{\partial P}\cdot\frac{\partial P}{\partial G}=\frac{\partial \mathrm{d}\dot{\varepsilon}}{\dot{\varepsilon}\mathrm{d}\sigma}=\left|\frac{\partial(\ln\sigma)}{\partial(\ln\dot{\varepsilon})}\right|_{\varepsilon,T} \quad (1)$$

For an ideal linear dissipater, m=1 and $J_{\max}=\sigma\dot{\varepsilon}/2$. The efficiency of power dissipation of a non-linear dissipater could be expressed as a dimensionless parameter [13]:

$$\eta=\frac{J}{J_{\max}}=\frac{2m}{m+1} \quad (2)$$

The variation of efficiency of power dissipation with temperature and strain rate gives the power dissipation map which is generally viewed as an iso-efficiency contour map and exhibits different domains correlated with specific microstructures.

The continuum instability criterion based on the extremum principle of irreversible thermodynamic was developed to identify the domains of flow instabilities, and given by another dimensionless parameter [13]:

$$\xi(\dot{\varepsilon}) = \frac{\partial \ln(\frac{m}{m+1})}{\partial \ln \dot{\varepsilon}} + m < 0 \quad (3)$$

The variation of the instability parameter as a function of temperature and strain rate represents an instability map which delineates regions of instability. The metallurgical instability during plastic flow occurred in these domains like adiabatic shear bands, flow localizations, cracking, kink bands, mechanical twinning and flow rotations.

A processing map can be constructed by superimposing the instability map over the power dissipation map. By using the processing map, the plastic deformation mechanisms in various deformation conditions can be predicted, and the unstable deformation regimes could also be avoided during hot deformation process.

Figure 3 shows the processing maps of the AA2014 alloy at strains of 0.1, 0.3, 0.5 and 0.7. The contour numbers indicate the efficiency of power dissipation, and the shaded region represents the instability domain. As shown in Fig. 3(a), at a strain of 0.1, there is no instability domain, while in Figs. 3(b), (c) and (d), the processing maps tend to exhibit a larger area instability domain with accumulation of strain, which mainly locates at the upper part of the processing maps. Moreover, the maximum efficiency value increases with increasing strain, which lies in the region with high temperature and low strain rate. This suggests that the degree of deformation has a significant impact on the workability of the AA2014 alloy. For the case of a strain of 0.7, an instability domain occurs at strain rates of 0.15−1 s^{-1} and the entire deformation temperatures. In addition, there exist two stability domains: domain I, with, lower efficiency of power dissipation (0.23−0.31), occurs at temperatures of 350−430 °C and intermediate strain rates of 0.005−0.1 s^{-1}; domain II, with higher efficiency of power dissipation (0.33−0.37), occurs at higher temperatures of 450−480 °C and strain rates of 0.001−0.05 s^{-1}. The contour lines in both of the stability domains are not very dense, which provides a relatively large window for safe processing.

3.3 Microstructure evolution

Figure 4 shows typical OM micrographs of the specimens deformed in different domains, among which

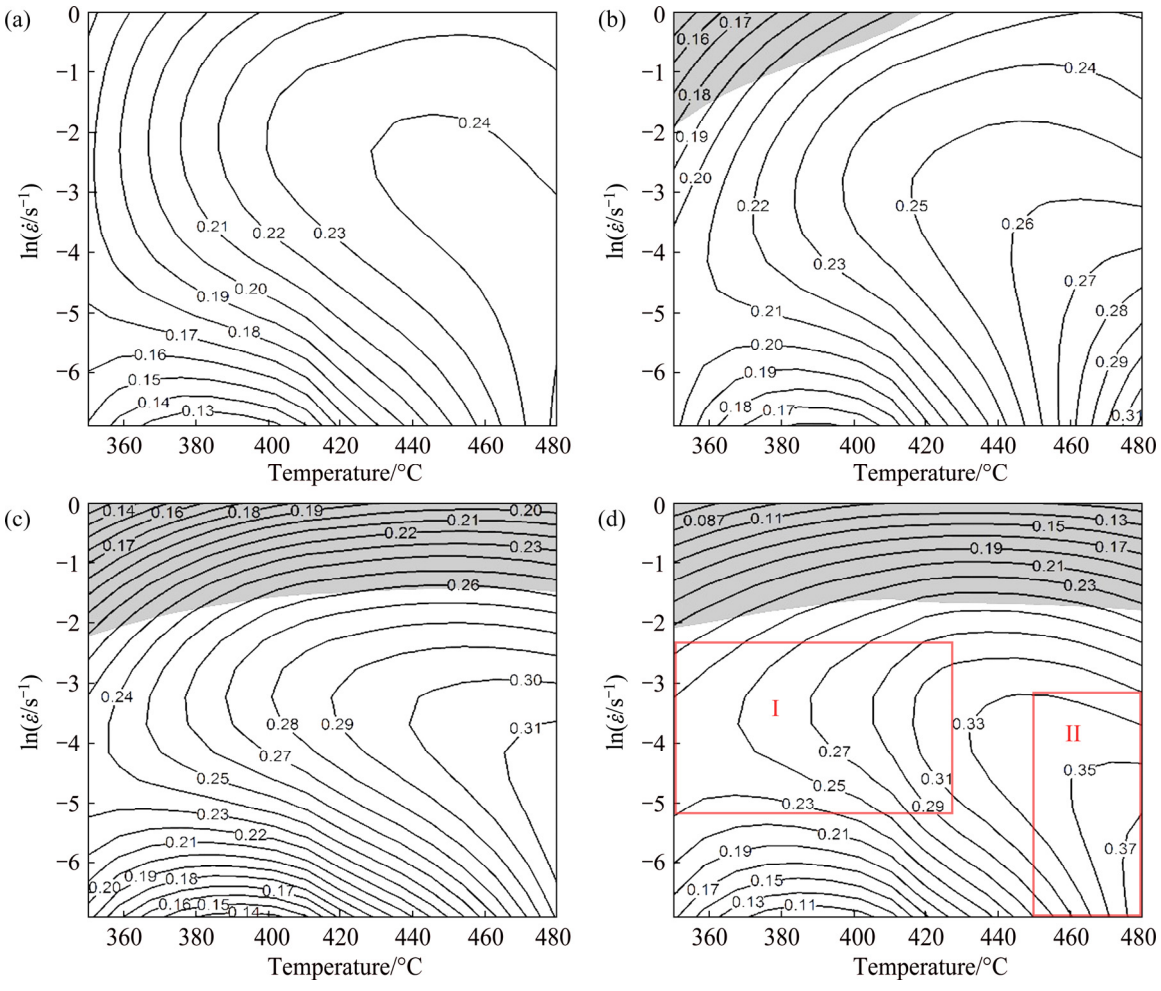

Fig. 3 Processing maps at different strains: (a) 0.1; (b) 0.3; (c) 0.5; (d) 0.7

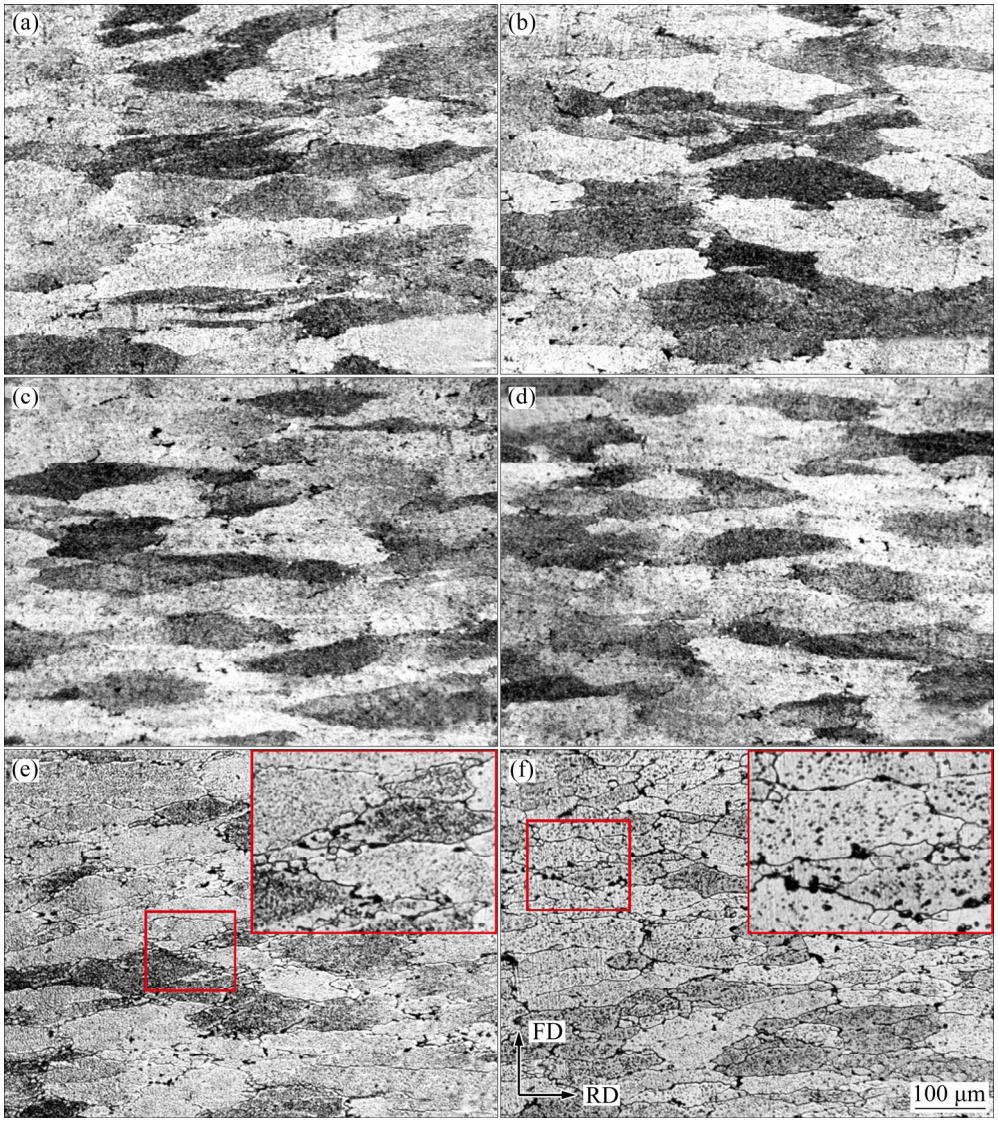

Fig. 4 Typical optical microstructures for different specimens deformed at different parameters: (a) 350 °C, 1 s^{-1}; (b) 450 °C, 1 s^{-1}; (c) 350 °C, 0.01 s^{-1}; (d) 400 °C, 0.1 s^{-1}; (e) 450 °C, 0.01 s^{-1}; (f) 480 °C, 0.001 s^{-1}

Figs. 4(a) and (b) are obtained in the instability domain; Figs. 4(c) and (d) are obtained in domain I; Figs. 4(e) and (f) are obtained in domain II. As shown in Fig. 4(a), highly elongated grains exist in the non-uniform microstructure, which are caused by local non-uniform deformation at high strain rate. With deformation temperature increasing to 450 °C, the local non-uniform deformation becomes less intense (Fig. 4(b)). Therefore, the flow instability occurs in the form of local non-uniform deformation rather than adiabatic shear bands or cracking, showing a good workability of the AA2014 aluminum alloy. In domain I (Figs. 4(c) and (d)), the flow localization disappears and the uniform elongated grains appear in the microstructures, which shows the typical features of dynamic recovery. This is because more slip systems are activated at higher deformation temperatures, which can make the deformation microstructure more homogeneous [14]. Furthermore, with further deformation carried out in domain II, the average grain size is much smaller and new fine equiaxed grains which might be sub-grains or recrystallized grains can be obviously observed in the microstructures (Figs. 4(e) and (f)). It can be interpreted that the atomic diffusion and the cross-slip of dislocation are reinforced at higher deformation temperatures; in addition, the movability of sub-grain boundaries is increased. Based on the processing maps, when the deformation is carried out from domain I to domain II, the efficiency value increases from 0.23 to 0.37. As we all know, the deformation mechanisms of the stability domains include DRV, DRX and super-plasticity. The consumption of energy storage in the process of DRX is higher than that in the process of DRV. Previous research has shown that the efficiency value is 20%−30% for DRV and 35%−45% for DRX [15].

The inverse pole figures (IPFs) of the deformed

specimens obtained by EBSD are shown in Fig. 5, among which Fig. 5(a) is associated to the instability domain; Figs. 5(b) and (c) are associated to stability domain I; Figs. 5(d) and (e) are associated to stability domain II. In all orientation maps, thin red line and thick black line represent low-angle grain boundaries (LAGBs, grain boundaries misorientation ≤15°) and high-angle grain boundaries (HAGBs, grain boundaries misorientation >15°), respectively. Generally, LAGBs correspond to the sub-grains obtained by DRV. While HAGBs correspond to the new grains obtained by DRX [16]. From these figures, it can be seen that the microstructures mostly consist of deformed grains and equiaxed grains characterized by HAGBs are not obviously observed. Figure 6 shows the boundary fractions of specimens obtained in different domains. With the change of deformation parameters (i.e., from domain I to domain II), a continuous decrease in LAGBs (2°−5°) and a steady increase in LAGBs (5°−15°) and HAGBs (30°−60°) are observed in Fig. 6. Such an evolution can be referred to as DRX according to the prior researches [17]. However, equiaxed grains are not obviously observed in the IPFs except a little movement of some grain boundaries particularly near the triple points (Fig. 5(e)) to reduce curvature, which is usually termed extended recovery. In domain II, high temperature and low strain rate mean that the diffusion abilities of atoms, cross-slip of dislocation and migration of grain boundaries are enhanced. Dislocations produced by strain hardening accumulate progressively at low-angle boundaries, leading to the increase of their misorientation angle and the gradual build-up of higher

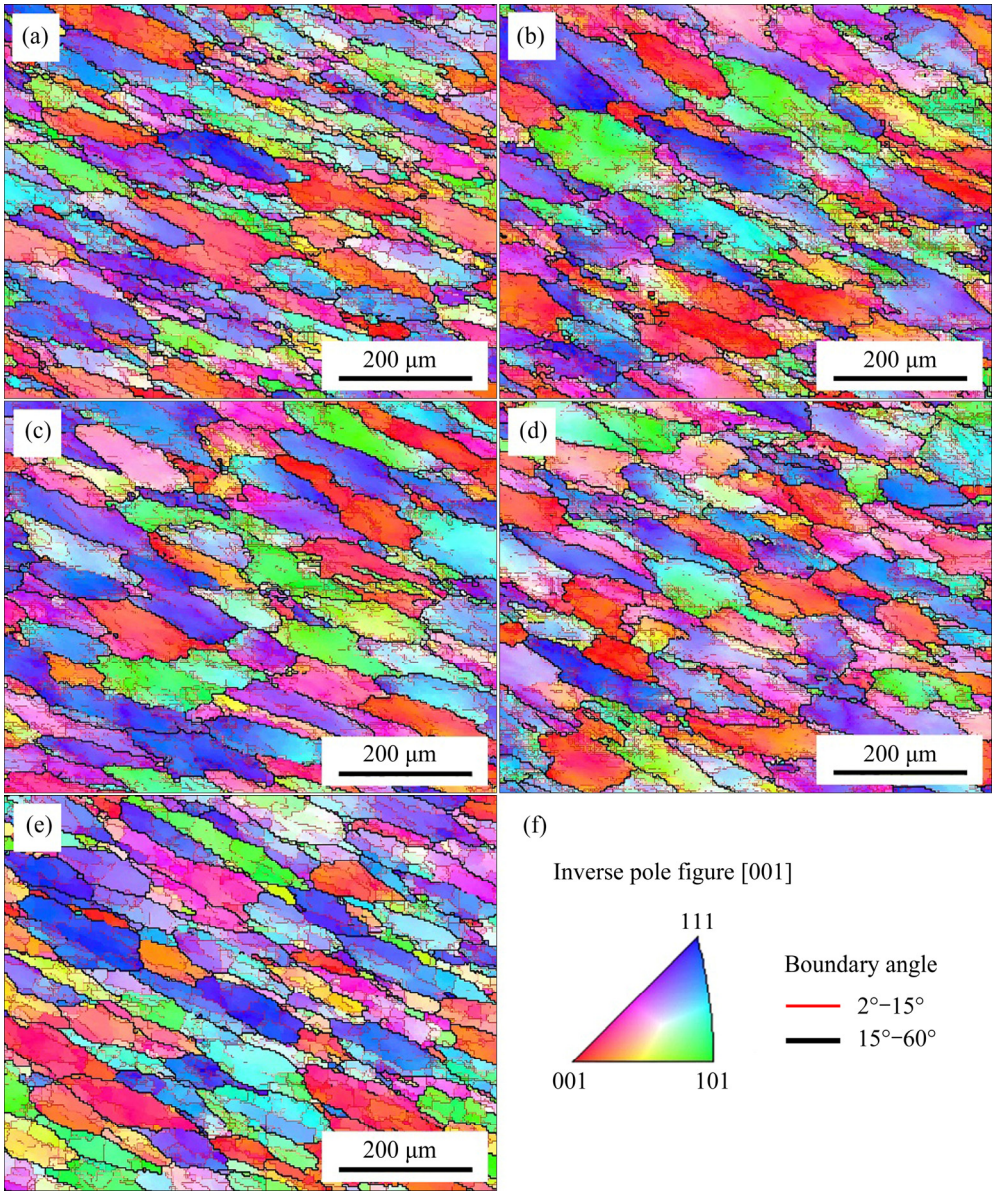

Fig. 5 IPF maps (a−e) and inverse pole figure (f) of specimens deformed under different parameters: (a) 350 °C, 1 s^{-1}; (b) 350 °C, 0.01 s^{-1}; (c) 400 °C, 0.1 s^{-1}; (d) 450 °C, 0.01 s^{-1}; (e) 480 °C, 0.001 s^{-1}; (f) Inverse pole figure

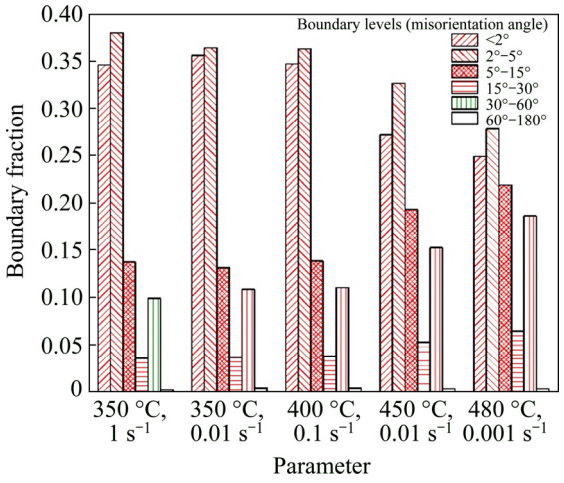

Fig. 6 Fractions of boundaries with different misorientation angles vs deformation parameters

misorientation boundaries between the neighbouring sub-grains. Thus, such a variation of the fractions of LAGBs and HAGBs may be caused by the extended recovery, which will lead to the transformation of sub-grain boundaries (Fig. 4(f)) into new high-angle grain boundaries (Fig. 5(e)). While according to Ref. [17], this is a potential continuous dynamic recrystallization (CDRX). Therefore, the predominant softening mechanism of the AA2014 aluminum alloy during hot compression is DRV.

Figure 7 shows the TEM images of the specimens deformed in different domains of the processing map. In the instability domain, the high strain rate obviously affects the microstructure evolution. It can be easily found that with dislocation tangles high density exists in the deformation structures, and some bending sub-grain boundaries are formed after the annihilation and

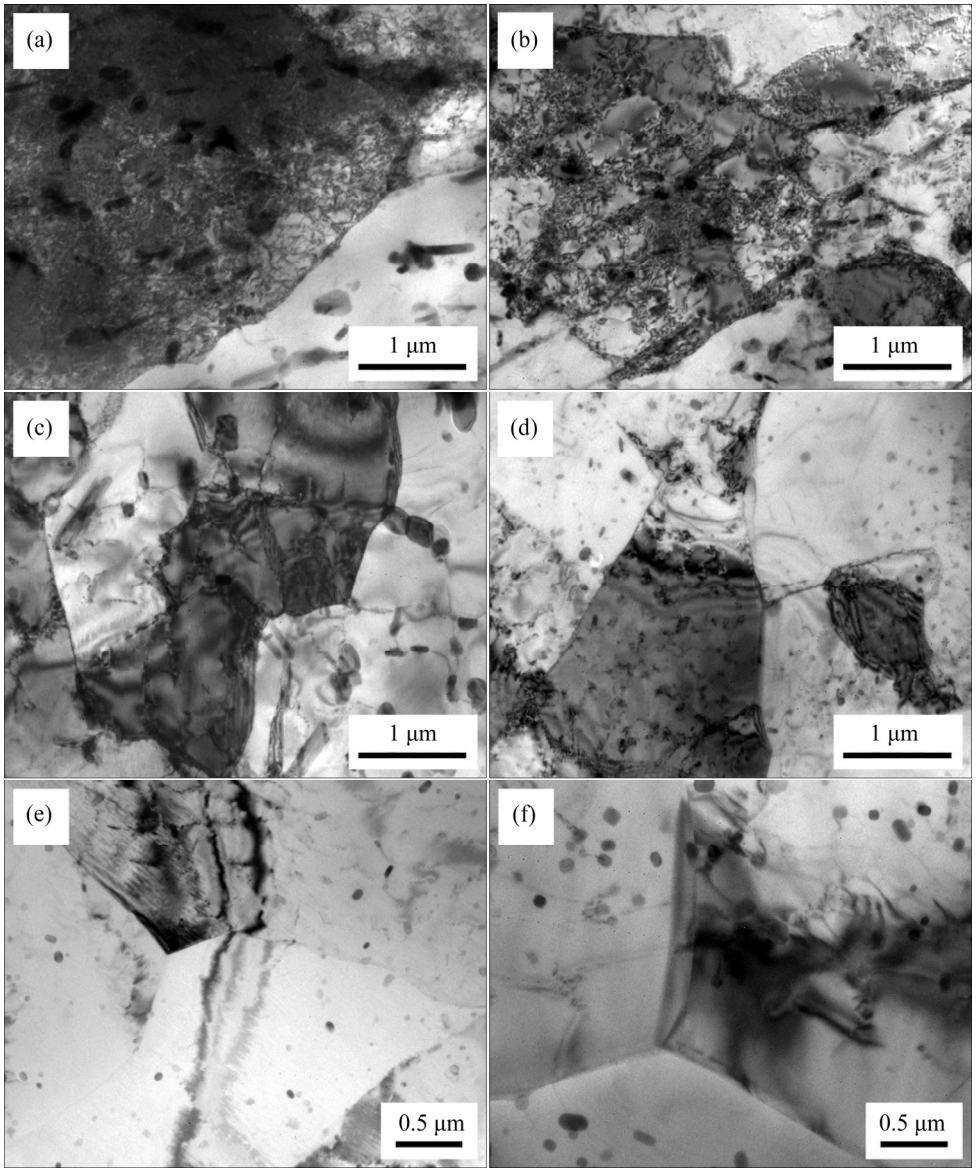

Fig. 7 TEM images of specimens deformed under different parameters: (a) 350 °C, 1 s^{-1}; (b) 450 °C, 1 s^{-1}; (c) 400 °C, 0.1 s^{-1}; (d) 450 °C, 0.01 s^{-1}; (e, f) 480 °C, 0.001 s^{-1}

recombination of the dislocations (Figs. 7(a) and (b)). Hence, the dynamic recovery process occurs during this period. In domain I, with increasing deformation temperature and/or decreasing strain rate, the dislocations reorganize through climbing and sliding, which leads to a decrease of the dislocation density and the formation of the dislocation wall (Fig. 7(c)). Thus, the DRV process is enhanced. With further deformation carried out in domain II, the grain boundaries become straight and clear (Fig. 7(d)). At a higher deformation temperature of 480 °C and lower strain rate of 0.001 s^{-1}, sufficient migration of metallic atoms and dislocations leads to the merging of some sub-grains. And the LAGBs can transform into HAGBs through absorbing dislocations. As a result, some high-angle boundary grains are formed (Figs. 7(e) and (f)).

From the above discussion, deformation temperatures and strain rates in different processing domains of the processing map have a remarkable effect on the microstructure evolution as well as the softening mechanism. And there is no doubt that the main softening mechanism of the homogenized AA2014 aluminum alloy is DRV in this study. A high DRV degree takes place in domain II with efficiency of power dissipation of 0.37. And low-angle boundary sub-grains progressively transform into high-angle boundary grains by extended recovery. Although the extended recovery is a beneficial process in hot deformation as it gives good development of a fine and misoriented microstructure, it needs the condition of a considerable strain to achieve a uniform and fine microstructure [17]. Therefore, domain I with relatively small efficiency of power dissipation and softening mechanism of DRV is more suitable for thermal processing.

3.4 Kinetic analysis

3.4.1 Strain compensated hyperbolic sine constitutive model

The Arrhenius equation including the Zener−Hollomon parameter is here to describe the flow behavior of the AA2014 aluminum alloy. The theory can be expressed as follows [18−21]:

$$Z = \dot{\varepsilon}\exp[Q/(RT)] \tag{4}$$

$$\dot{\varepsilon} = A_1\sigma^{n_1}\exp[-Q/(RT)],\ \alpha\sigma<0.8 \tag{5}$$

$$\dot{\varepsilon} = A_2\exp(\beta\sigma)\exp[-Q/(RT)],\ \alpha\sigma>1.2 \tag{6}$$

$$\dot{\varepsilon} = A[\sinh(\alpha\sigma)]^n\exp[-Q/(RT)],\ \text{for all } \sigma \text{ level} \tag{7}$$

where A, A_1, A_2, n_1, n, β and α are material constants, $\alpha=\beta/n_1$, $\dot{\varepsilon}$ is the strain rate, Q is the activation energy for deformation, R is the mole gas constant, and T is the deformation temperature.

It is commonly accepted that the effect of strain on stress will not be considered in Eqs. (4)−(7). In this study, the effects of deformation strain on the material constants were investigated by establishment of the Arrhenius-type constitutive model considering strain compensation. The material constants of the constitutive model were evaluated using stress−strain data from compression tests. As an example, the solution procedure of the material constants at the strain of 0.1 is illustrated below.

Taking logarithm from both sides of Eqs. (5) and (6) yields:

$$\ln\dot{\varepsilon} = \ln A_1 + n_1\ln\sigma - Q/(RT) \tag{8}$$

$$\ln\dot{\varepsilon} = \ln A_1 + \beta\sigma - Q/(RT) \tag{9}$$

The material constants n_1 and β can be obtained from the mean slope of the lines in $\ln\dot{\varepsilon}-\ln\sigma$ and $\ln\dot{\varepsilon}-\sigma$ plots, respectively, as shown in Fig. 8 (a) and (b), respectively. Thus, mean values of n_1 and β can be computed as 9.0354 and 0.1484 MPa^{-1}, respectively, then $\alpha=\beta/n_1=0.188$ MPa^{-1}.

Taking differential transformation of Eq. (7), the following relation is obtained:

$$Q = R\left\{\frac{\partial\ln\dot{\varepsilon}}{\partial\ln[\sinh(\alpha\sigma)]}\right\}_T\left\{\frac{\partial\ln[\sinh(\alpha\sigma)]}{\partial(1/T)}\right\}_{\dot{\varepsilon}} \tag{10}$$

From Eq. (10), we can know that Q can be calculated from the mean slope of the lines in $\ln\dot{\varepsilon}-\ln[\sinh(\alpha\sigma)]$ and $\ln[\sinh(\alpha\sigma)]-1000/T$ plots at various temperatures and strain rates, as shown in Figs. 8(c) and (d) , respectively. Thus, the mean value of Q is 201.078 kJ/mol.

From Eqs. (4) and (7), it can be expressed as

$$Z = A[\sinh(\alpha\sigma)]^n \tag{11}$$

Taking logarithm from both sides of Eq. (11), it can be obtained:

$$\ln Z = \ln A + n\ln[\sinh(\alpha\sigma)] \tag{12}$$

Obviously, the values of $\ln A$ and n are the intercept and slope of the line in $\ln Z-\ln[\sinh(\alpha\sigma)]$ plot, respectively. It is easy to evaluate the values of $\ln A$ and n as 30.6746 and 6.4703, respectively.

The flow stress σ can be written as a function of Zener−Hollomon parameter, considering the definition of the hyperbolic law:

$$\sigma = \frac{1}{\alpha}\ln\left\{\left(\frac{z}{A}\right)^{1/n} + \left[\left(\frac{z}{A}\right)^{2/n}+1\right]^{1/2}\right\} \tag{13}$$

Then, material constants Q, A, n and α at every interval of 0.05 in the strain range of 0.05−0.6 are obtained by repeating the above procedures. The relationships between Q, $\ln A$, n, α and true strain are five-order polynomial fitted by the compensation of strain. The polynomial fit results Q, $\ln A$, n and α are provided in Table 2. Based on the experimental results, the constitutive equations that describe the flow stress as

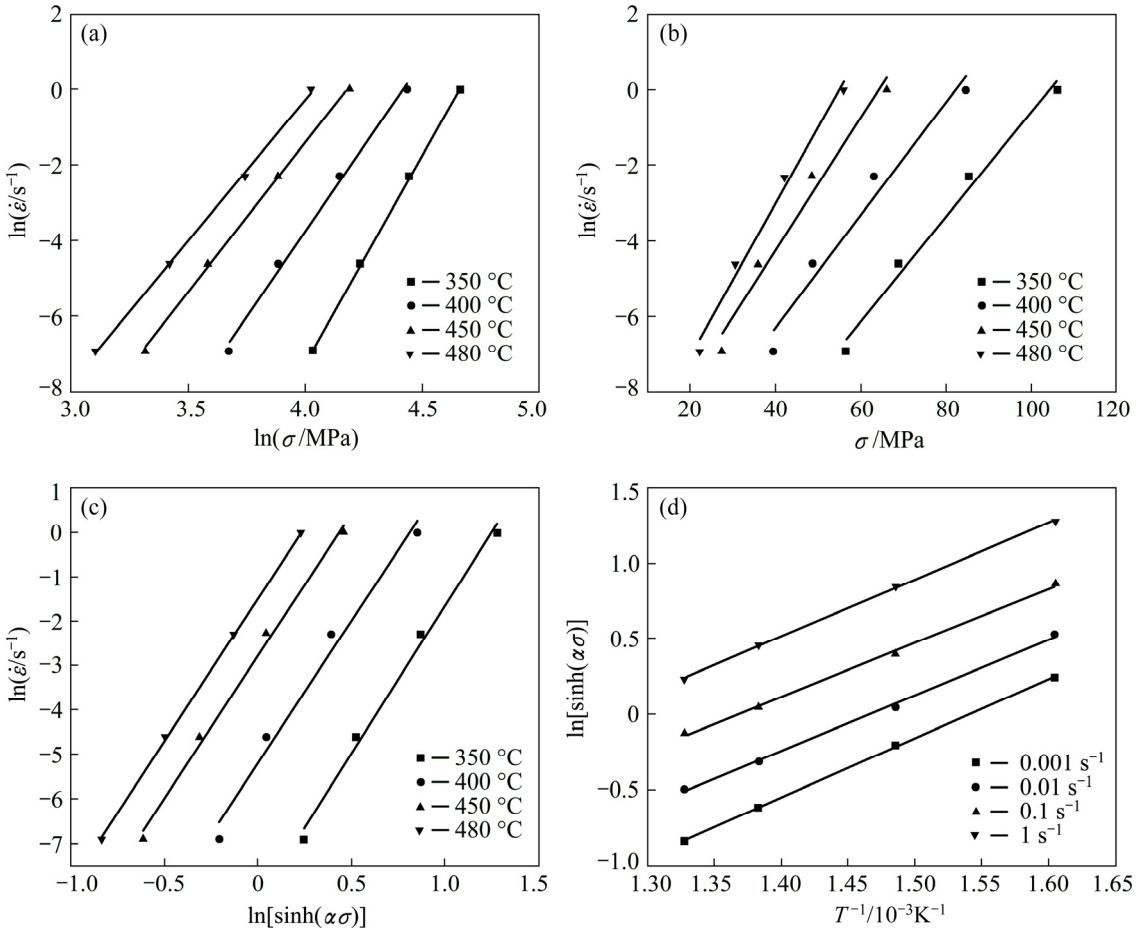

Fig. 8 Relationships between $\ln \dot{\varepsilon}$ and $\ln \sigma$ (a), $\ln \dot{\varepsilon}$ and σ (b), $\ln \dot{\varepsilon}$ and $\ln[\sinh(\alpha\sigma)]$ (c), $\ln[\sinh(\alpha\sigma)]$ and $1000/T$ (d)

a function of strain rate, deformation temperature and strain can be written as

$$\begin{cases} \sigma = \dfrac{1}{\alpha}\ln\left\{\left(\dfrac{z}{A}\right)^{1/n} + \left[\left(\dfrac{z}{A}\right)^{2/n} + 1\right]^{1/2}\right\} \\ Z = \dot{\varepsilon}\exp[Q/(RT)] \\ Q = B_0 + B_1\varepsilon + B_2\varepsilon^2 + B_3\varepsilon^3 + B_4\varepsilon^4 + B_5\varepsilon^5 \\ \ln A = C_0 + C_1\varepsilon + C_2\varepsilon^2 + C_3\varepsilon^3 + C_4\varepsilon^4 + C_5\varepsilon^5 \\ n = D_0 + D_1\varepsilon + D_2\varepsilon^2 + D_3\varepsilon^3 + D_4\varepsilon^4 + D_5\varepsilon^5 \\ \alpha = E_0 + E_1\varepsilon + E_2\varepsilon^2 + E_3\varepsilon^3 + E_4\varepsilon^4 + E_5\varepsilon^5 \end{cases} \tag{14}$$

Table 2 Polynomial fit results of Q, $\ln A$, n and α of AA2014 aluminum alloy

Q		$\ln A$		n		α	
B_0	215.736	C_0	33.334	D_0	6.882	E_0	0.018
B_1	−222.841	C_1	−39.661	D_1	−1.784	E_1	0.008
B_2	915.813	C_2	157.425	D_2	−37.436	E_2	−0.025
B_3	−2508.337	C_3	−423.232	D_3	170.035	E_3	0.044
B_4	2929.401	C_4	496.423	D_4	−288.720	E_4	−0.081
B_5	−1114.806	C_5	−192.990	D_5	173.067	E_5	0.066

3.4.2 Verification of constitutive model

In order to evaluate the accuracy of the strain compensated constitutive model, the correlation coefficient R_1 and the absolute average relatively error (AARE) can be calculated as follows [22]:

$$R_1 = \frac{\sum_{i=1}^{n}(E_i - \bar{E})(P_i - \bar{P})}{\sqrt{\sum_{i=1}^{n}(E_i - \bar{E})^2 \sum_{i=1}^{n}(P_i - \bar{P})^2}} \tag{15}$$

$$\text{AARE} = \frac{1}{n}\sum_{i=1}^{n}\left|\frac{E_i - P_i}{E_i}\right| \times 100\% \tag{16}$$

where E is the experimental data, P is the predicted data, $\bar{E}$ and $\bar{P}$ are average values, n is the number of data. The temperature corrected data and the predicted data are linearly fitted as shown in Fig. 9. Thus, the values of R_1 and AARE are 0.9959 and 1.8%, respectively. The result indicates that the proposed strain compensated constitutive model shows an accurate estimate of the flow stress for AA2014 aluminum alloy in the deformation temperature range of 350−480 °C and strain rate range of 0.001−1 s^{-1}.

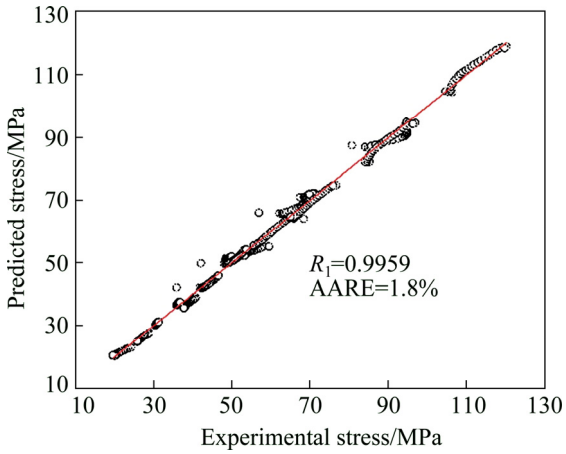

Fig. 9 Correlation between experimental and predicted flow stress data

3.4.3 Activation energy map

One of the most notable characteristics during hot deformation of metallic materials is that the microstructure evolution is controlled by thermal activation. The activation energy for deformation is related to the dominant softening mechanism. Dynamic recovery behavior is considered to be associated with dislocation climbing and cross-slipping for dislocation rearrangement and elimination, which is diffusion-controlled. Therefore, it has been recognized that activation energy for deformation undergoing DRV is close to the self-diffusion activation energy; but for deformation accompanied by DRX, activation energy has been elevated to a higher level due to sub-grain nucleation and high-angle boundary migration. Activation energy Q for deformation, which is related to strain rate, deformation temperature and strain, is given by

$$Q=RT\{\ln A+n\ln[\sinh(\alpha\sigma)]-\ln\dot{\varepsilon}\} \quad (17)$$

where A, n and α are material constants, R is the mole gas constant. The variation of Q as a function of temperature and strain rate gives an activation energy map.

Figure 10 shows the activation energy map for the AA2014 aluminum alloy at the strain of 0.7. It varies in the range of 160.9−164.7 kJ/mol. These values are higher than the self-diffusion energy of pure aluminum (i.e., 142 kJ/mol [23]) to a small extent. This should be due to the pinning effect of the dispersion particles on the motion of dislocations. The dispersion particles precipitated during slow cooling from the high temperature of homogenization in the bulk of industrial AA2014 aluminum alloy (Figs. 1 and 7). On the basis of the concept of activation energy, MALAS and SEETHARAMAN [24] introduced the activation energy map to identify the processing window for hot working. According to Ref. [24], the desirable domain for safe working corresponds to the region where activation energy is relatively constant in the activation energy map. As shown in Fig. 10, the marked square region, where Q is relatively constant in the range of 160.9−161.4 kJ/mol, consists of the optimum deformation parameters for obtaining a single and homogeneous microstructure with a sole deformation mechanism of DRV. Therefore, combined with the conclusion in microstructure evolution, the optimum deformation domain for the homogenized AA2014 aluminum alloy might be the deformation temperature range of 370−420 °C and strain rate range of 0.008−0.08 s^{-1} with efficiency of power dissipation of 0.25−0.3.

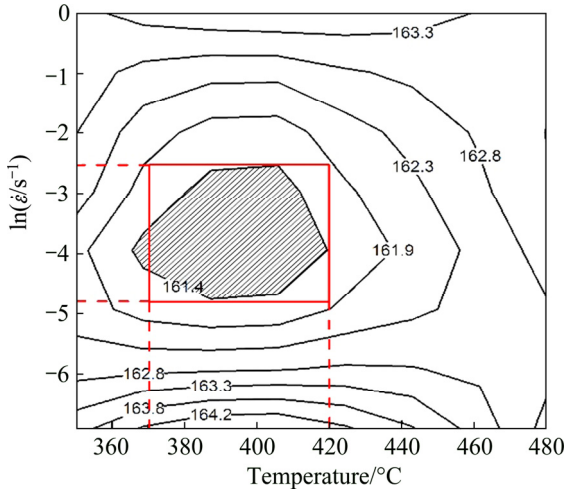

Fig. 10 Activation energy map at strain of 0.7 (unit: kJ/mol)

4 Conclusions

1) The accumulation of strain increases the range of flow instability domain which occurs at the upper part of the processing maps with instability in the form of local non-uniform deformation.

2) At the strain of 0.7, there exist two stability domains: domain I (350−430 °C, 0.005−0.1 s^{-1}), with lower efficiency values of 0.23−0.31; domain II (450−480 °C, 0.001−0.05 s^{-1}), with higher efficiency values of 0.33−0.37. The predominant softening mechanisms in both of the two domains are dynamic recovery.

3) Uniform microstructures are obtained in domain I where dynamic recovery is the only softening mechanism. An extended recovery occurs in domain II, which will lead to the potential sub-grain boundaries progressively transforming into new high-angle grain boundaries.

4) A strain compensated Arrhenius-type constitutive model is established. The activation energy at the strain of 0.7 varies in the range of 160.9−164.7 kJ/mol.

5) The optimum deformation domain for the

homogenized AA2014 forging aluminum alloy is the deformation temperature range of 370−420 °C and the strain rate range of 0.008−0.08 s^{-1} with the power dissipation efficiency range of 0.25−0.3 and the activation energy range of 160.9−161.4 kJ/mol.

References

[1] DHAL A, PANIGRAHI S K, SHUNMUGAM M S. Precipitation phenomena, thermal stability and grain growth kinetics in an ultra-fine grained Al2014 alloy after annealing treatment [J]. Journal of Alloys and Compounds, 2015, 649: 229−238.

[2] LIANG Xiao-peng, LI Hui-zhong, HUANG Lan, HONG Tao, MA Bing, LIU Yong. Microstructural evolution of 2519-T87 aluminum alloy obliquely impacted by projectile with velocity of 816 m/s [J]. Transactions of Nonferrous Metals Society of China, 2012, 22: 1270−1279.

[3] LIN Yong-cheng, CHEN Xiao-min. A critical review of experimental results and constitutive descriptions for metals and alloys in hot working [J]. Materials and Design, 2011, 32(4): 1733−1759.

[4] ZHANG Tian, TAO You-rui, WANG Xue-yin. Constitutive behavior, microstructural evolution and processing map of extruded Al−1.1Mn−0.3Mg−0.25RE alloy during hot compression [J]. Transactions of Nonferrous Metals Society of China, 2014, 24: 1337−1345.

[5] WANG Ming-liang, JIN Pei-peng, WANG Jin-hui, HAN Li. Hot deformation behavior of as-quenched 7005 aluminum alloy [J]. Transactions of Nonferrous Metals Society of China, 2014, 24: 2796−2804.

[6] LIU Xiao-yan, PAN Qing-lin, HE Yun-bin, LI Wen-bin, LIANG Wen-Jie, YIN Zhi-min. Flow behavior and microstructural evolution of Al−Cu−Mg−Ag alloy during hot compression deformation [J]. Materials Science and Engineering A, 2009, 500(1−2): 150−154.

[7] CHEN Song-yi, CHEN Kang-hua, PENG Guo-sheng, CHEN Xue-hai, CENG Qing-hua. Effect of heat treatment on hot deformation behavior and microstructure evolution of 7085 aluminum alloy [J]. Journal of Alloys and Compounds, 2012, 537: 338−345.

[8] LIU Wen-yi, ZHAO Huan, LI Dan, ZHANG Zhi-qing, HUANG Guang-jie, LIU Qing. Hot deformation behavior of AA7085 aluminum alloy during isothermal compression at elevated temperature [J]. Materials Science and Engineering A, 2014, 596(24): 176−182.

[9] JIN Jun-song, WANG Xin-yun, HU Hui-e, XIA Ju-chen. High-temperature deformation behavior and processing map of 7050 aluminum alloy [J]. Metals and Materials International, 2012, 18(1): 69−75.

[10] LIN Yong-cheng, LI Lei-ting, XIA Yu-chi, JIANG Yu-qiang. Hot deformation and processing map of a typical Al−Zn−Mg−Cu alloy [J]. Journal of Alloys and Compounds, 2013, 550: 438−445.

[11] LI Bo, PAN Qing-lin, YIN Zhi-min. Characterization of hot deformation behavior of as-homogenized Al−Cu−Li−Sc−Zr alloy using processing map [J]. Materials Science and Engineering A, 2014, 618(22): 199−206.

[12] PRASAD Y V R K, GEGEL H L, DORAIVELU S M, MALAS J C, MORGAN J T, LARK K A, BARKER D R. Modeling of dynamic material behavior in hot deformation: Forging of Ti−6242 [J]. Metallurgical Transactions A, 1984, 15(10): 1883−1892.

[13] BOZZINI B, CERRI E. Numerical reliability of hot working processing maps [J]. Materials Science and Engineering A, 2011, 328(1−2): 344−347.

[14] SAKAI T, BELYAKOV A, KAIBYSHEV R, MIURA H, JONAS J J. Dynamic and post-dynamic recrystallization under hot, cold and severe plastic deformation conditions [J]. Progress in Materials Science, 2014, 60: 130−207.

[15] ZHEN Liang, HU Hui-e, WANG Xin-yun, ZHANG Bao-you, SHAO Wen-zhu. Distribution characterization of boundary misorientation angle of 7050 aluminum alloy after high-temperature compression [J]. Journal of Materials Processing Technology, 2009, 209(2): 754−761.

[16] BRANDON D G. The structure of high-angle grain boundaries [J]. Acta Metallurgica, 1966, 14(11): 1479−1487.

[17] GOURDET S, MONTHEILLET F. A model of continuous dynamic recrystallization [J]. Acta Materialia, 2003, 51(9): 2685−2699.

[18] DEHGHAN H, ABBASI S M, MOMENI A, KARIMI TAHERI A. On the constitutive modeling and microstructural evolution of hot compressed A286 iron-base super-alloy [J]. Journal of Alloys and Compounds, 2013, 564: 13−19.

[19] JI Guo-liang, LI Fu-guo, LI Qing-hua, LI Hui-qu, LI zhi. A comparative study on Arrhenius-type constitutive model and artificial neural network model to predict high-temperature deformation behaviour in Aermet100 steel [J]. Materials Science and Engineering A, 2011, 528(13−14): 4774−4782.

[20] MCQUEEN H J, IMBERT C A C. Dynamic recrystallization: Plasticity enhancing structural development [J]. Journal of Alloys and Compounds, 2004, 378(1−2): 35−43.

[21] SELLARS C M, MCTEGART W J. On the mechanism of hot deformation [J]. Acta Metallurgica, 1966, 14(11): 1136−1138.

[22] SAMANTARAY D, MANDAL S, BHADURI A K. Constitutive analysis to predict high-temperature flow stress in modified 9Cr−1Mo (P91) steel [J]. Materials and Design, 2010, 31(2): 981−984.

[23] CEPEDA-JIMENEZ C M, RUANO O A, CARSI M, CARRENO F. Study of hot deformation of an Al−Cu−Mg alloy using processing maps and microstructural characterization [J]. Materials Science and Engineering A, 2012, 552(2): 530−539.

[24] MALAS J C, SEETHARAMAN V. Using material behavior models to develop process control strategies [J]. The Journal of the Minerals, Metals and Materials Society, 1992, 44(6): 8−13.

应用加工图表征 AA2014 锻造铝合金的热变形行为

李鹏伟[1]，李慧中[1,2,3]，黄 岚[3]，梁霄鹏[1,2]，朱泽晓[1]

1. 中南大学 材料科学与工程学院，长沙 410083；
2. 中南大学 有色金属材料科学与工程教育部重点实验室，长沙 410083；
3. 中南大学 粉末冶金国家重点实验室，长沙 410083

摘 要：通过等温压缩试验研究 AA2014 锻造铝合金的热变形行为。试验在 Gleeble−3180 热模拟机上进行，温度和应变速率范围分别为 350~480 °C 和 0.001~1 s^{-1}。利用金相显微镜(OM)、电子背散射衍射(EBSD)、透射电子显微镜(TEM)等分析手段观察合金在不同变形条件下的显微组织，并构建应变为 0.1、0.3、0.5 和 0.7 时的加工图。结果表明：高应变速率(> 0.1 s^{-1})时易出现失稳变形区，并以局部不均匀变形为主要失稳形式。当应变为 0.7 时，加工图中存在两个稳定变形区：I 区(350~430 °C，0.005~0.1 s^{-1})和Ⅱ区(450~480 °C，0.001~0.05 s^{-1})，其主要软化机制均为动态回复。在变形区 I 中得到均匀的显微组织，在变形区Ⅱ中发生扩展回复，这将导致潜在的亚晶界逐步转变为新的大角度晶界。AA2014 锻造铝合金的最佳热加工参数如下：温度 370~420 °C，应变速率 0.008~0.08 s^{-1}。

关键词：AA2014 铝合金；热变形行为；本构模型；加工图；软化机制

(Edited by Wei-ping CHEN)